

# Amplified spontaneous emission and photoresponse characteristics in highly defect tolerant $\text{CsPbCl}_x\text{Br}_{3-x}$ crystal

LONGXING SU,<sup>1,2,\*</sup> BINGHENG MENG,<sup>3</sup> HENG LI,<sup>2</sup> ZHUO YU,<sup>2</sup> YUAN ZHU,<sup>2,5</sup> AND RUI CHEN<sup>4,6</sup>

<sup>1</sup>International School of Microelectronics, Dongguan University of Technology, Dongguan 523808, China

<sup>2</sup>School of Microelectronics, Southern University of Science and Technology, Shenzhen 518055, China

<sup>3</sup>State Key Laboratory of High Power Semiconductor Laser, School of Physics, Changchun University of Science and Technology, Changchun 130022, China

<sup>4</sup>Department of Electrical and Electronic Engineering, Southern University of Science and Technology, Shenzhen 518055, China

<sup>5</sup>e-mail: zhuy3@sustech.edu.cn

<sup>6</sup>e-mail: chenr@sustech.edu.cn

\*Corresponding author: sulongxing@dgut.edu.cn

Received 16 August 2024; revised 23 October 2024; accepted 11 November 2024; posted 13 November 2024 (Doc. ID 539352); published 9 January 2025

All inorganic perovskite  $\text{CsPbX}_3$  with excellent optical properties and a tunable bandgap is a potential candidate for optoelectronic applications, and the amplified spontaneous emission (ASE) is normally reported in low-dimensional structures where the quantum confinement enhances ASE. Herein, we not only demonstrate the ASE in millimeter size  $\text{CsPbCl}_x\text{Br}_{3-x}$  crystal with a high defect concentration, but also tune the emission wavelength from the green band to blue band through the ion exchange of Br with Cl. The ASE centered at  $\sim 456$  nm is probed at 50 K with a threshold of  $106 \mu\text{J}/\text{cm}^2$ . Furthermore, a metal-semiconductor-metal (MSM) structure  $\text{CsPbCl}_x\text{Br}_{3-x}$  photodetector is fabricated and shows a distinct response to lights from UV to the blue band; the response spectrum range is quite different from the narrow band ( $\sim 30$  nm) response of the  $\text{CsPbBr}_3$  photodetector induced by a charge collection narrowing (CCN) mechanism. The  $\text{CsPbCl}_x\text{Br}_{3-x}$  photodetector also exhibits fast response speeds with a rise time of  $96 \mu\text{s}$  and a decay time of  $34 \mu\text{s}$ , indicating the defects have limited influence on the transportation speed of the photo-generated carriers. © 2025 Chinese Laser Press

<https://doi.org/10.1364/PRJ.539352>

## 1. INTRODUCTION

Recently, all inorganic lead halide perovskites ( $\text{CsPbX}_3$ ,  $X = \text{Cl}$ ,  $\text{Br}$ ,  $\text{I}$ ) have received tremendous attention in optoelectronic devices because of their advantages including a large light absorption coefficient, low fabrication cost, tunable bandgap, and high carrier mobility [1–3]. The most interesting feature of this group of material is the ability to obtain high optical gain in the whole visible range, making them highly desirable in tunable lasers, broad band amplifiers, and response band adjustable photodetectors [4–6]. Generally, mixed halide perovskites ( $\text{CsPbCl}_x\text{Br}_{3-x}$  or  $\text{CsPbBr}_x\text{I}_{3-x}$ ) can be prepared by adding or mixing appropriate  $\text{PbX}_2$  salts as precursors; thus the bandgap is correspondingly modulated from near ultraviolet (UV) to the red spectrum through fast anion exchange [7]. Huang *et al.* have synthesized a series of  $\text{CsPbCl}_x\text{Br}_{3-x}$  ( $x = 0–2.5$ ) samples with emission wavelength from 525 nm to 430 nm through a solution method [8]. A vapor-assisted post-synthesis chlorination procedure is another efficient strategy to convert the green emitting  $\text{CsPbBr}_3$  into blue emitting  $\text{CsPbCl}_x\text{Br}_{3-x}$  through controlling

the conversion temperature and time [9]. Typically, the low-dimensional structures like quantum dots, nanocrystals, and microplates are promising in realizing the low-threshold amplified spontaneous emission (ASE) because of the quantum confinement effect [10].  $\text{CsPbCl}_x\text{Br}_{3-x}$  quantum dots and nanofilm have proved their ASE behavior with pumping thresholds of  $20–56 \mu\text{J}/\text{cm}^2$ , and the ASE peak centers are tuned to the blue band (440–495 nm) [11–13]. Compared with the low-dimensional structures, a large sized crystal is more difficult in the realization of ASE but has more potential in practical application. Kim *et al.* report the one-photon pumped ASE in  $\text{CsPbBr}_3$  single crystals, while the limited penetration depth and reabsorption of the crystal induce a large threshold of  $1.38 \text{ mJ}/\text{cm}^2$  [14]. Zhao *et al.* reduce the ASE threshold ( $0.65 \text{ mJ}/\text{cm}^2$ ) in millimeter sized  $\text{CsPbBr}_3$  crystal using two-photon excitation, but the full width at half maximum (FWHM) is as large as 7 nm [15]. To date, studies regarding blue band ASE in millimeter sized lead halide perovskites are still rare. On the other side, as another kind of optoelectronic device that can convert the light into electrical

signal, an all inorganic lead halide perovskite ( $\text{CsPbX}_3$ ,  $X = \text{Cl}$ ,  $\text{Br}$ ,  $\text{I}$ ) photodetector plays a key role in optical imaging, environmental monitoring, forest fire alarms, and space secure communication [16–18]. However, a strong and narrow response band is normally observed in single crystal perovskites [19,20], which can be attributed to the CCN mechanism [21]. Therefore, it is highly desired if a low-threshold ASE and broadband photoreponse can be simultaneously realized within a large sized  $\text{CsPbX}_3$  crystal.

In this work, millimeter sized  $\text{CsPbCl}_x\text{Br}_{3-x}$  crystals are synthesized through a simple anti-solvent process at room temperature. High surface defect density is observed and determined in the as-prepared sample with low photoluminescence quantum yield (PLQY) of only 0.35%. Nevertheless, ASE behavior still can be observed with a relatively low threshold of  $106 \mu\text{J}/\text{cm}^2$  at 50 K, which verifies the high defect tolerance of the all inorganic perovskite. In addition, compared with the emission center of  $\text{CsPbBr}_3$  crystal, the ASE emission peak blue shifts from  $\sim 529$  to  $\sim 456$  nm because of the anion exchange of  $\text{Br}$  by  $\text{Cl}$ . Subsequently, a symmetric MSM type photodetector based on  $\text{CsPbCl}_x\text{Br}_{3-x}$  is prepared with  $\text{InGa}$  as the Ohmic contact. At 10 V, the photodetector demonstrates good performances with a responsivity of  $3.95 \text{ mA}/\text{W}$ , a detectivity of  $7 \times 10^{10}$  Jones, and fast response speeds of  $96 \mu\text{s}$  (rise time) and  $34 \mu\text{s}$  (decay time).

## 2. EXPERIMENTAL SECTION

### A. Chemicals and Reagents

Cesium bromide ( $\text{CsBr}$ , 99.9%), cesium chloride ( $\text{CsCl}$ , 99.9%), and lead bromide ( $\text{PbBr}_2$ , 99.9%) were purchased from Alfa Aesar (China) Co., Ltd. Dimethyl sulfoxide (DMSO, 99.5%), methanol (99.5%), and ethanol (99.5%) were purchased from Sinopharm Chemical Reagent Co., Ltd. All reagents and solvents were used without any purification.

### B. Synthesis of $\text{CsPbCl}_x\text{Br}_{3-x}$ Crystals

The  $\text{CsPbCl}_x\text{Br}_{3-x}$  sample was synthesized by an infiltrating inverse solvent re-crystallization method. 0.93 g  $\text{CsBr}$ , 0.93 g  $\text{CsCl}$ , and 0.93 g  $\text{PbBr}_2$  were simultaneously loaded in 8 mL DMSO solution and then stirred for 1 h. After precipitating for 1 h, the supernatant was transferred into a vial, and then the vial was loaded inside a beaker filled with methanol. Subsequently, the beaker was sealed by paraffin film in order to maintain the methanol atmosphere. The growth temperature is at room temperature, and yellow  $\text{CsPbCl}_x\text{Br}_{3-x}$  crystals were obtained after 5 days. Finally, the  $\text{CsPbCl}_x\text{Br}_{3-x}$  crystals were washed by ethanol and dried in the oven at  $60^\circ\text{C}$  for 30 min. It is worth noting that the repeatability of the method at a small-batch scale (gram scale) is good.  $\text{CsPbCl}_x\text{Br}_{3-x}$  crystals with the similar size and the same component ratio can be collected within different batches under the same growth parameters. According to a previous study on the production of kilogram-scale  $\text{PbI}_2$  crystals using the similar solution method [22], large-scale production of  $\text{CsPbCl}_x\text{Br}_{3-x}$  crystals for practical applications is expected with the upgrade and expansion of the synthesized facilities.

### C. Characterizations

The XRD pattern of the  $\text{CsPbCl}_x\text{Br}_{3-x}$  sample was collected using a multifunctional X-ray diffractometer (XRD, Bruker, D8 Advance) with a  $\text{Cu-K}\alpha$  line ( $1.54 \text{ \AA}$ ). The Raman spectrum of the  $\text{CsPbCl}_x\text{Br}_{3-x}$  sample was excited by a 532 nm laser and collected through a back scattering configuration. The room temperature photoluminescence (PL) spectrum was measured to study the luminescence behavior of the  $\text{CsPbCl}_x\text{Br}_{3-x}$  sample. The photoluminescence quantum yield (PLQY) was determined (Edinburgh Instruments, FLS-1000) to study the PL efficiency of  $\text{CsPbCl}_x\text{Br}_{3-x}$ . X-ray photoelectron spectroscopy (XPS, Thermo Fisher Scientific, ESCALAB XI) and ultraviolet photoelectron spectroscopy (UPS) were used to investigate the chemical state and energy band structure.

### D. ASE Measurement

A 355 nm laser (100 fs, 1 kHz) with different densities was used as the excitation source to excite the  $\text{CsPbCl}_x\text{Br}_{3-x}$  sample. The measurements were conducted at both room temperature and 50 K. Temperature-dependent PL spectra under excitation density of  $5.9 \mu\text{J}/\text{cm}^2$  were also collected. During the measurement, the emission was collected by a spectrometer with resolution of 0.09 nm (Princeton Instrument, SpectraPro HRS-300).

### E. Device Fabrication and Measurement

$\text{InGa}$  electrodes were employed as the contact electrodes for the  $\text{CsPbCl}_x\text{Br}_{3-x}$  MSM photodetector. The response characteristics of the device were investigated by using an electrochemical workstation (Ivium Vertex One). A Xe-lamp equipped with a monochromator was utilized as the excitation source. The photoresponse measurements were performed in an air environment with a relative humidity (RH) of  $\sim 57\%$ . The time-resolved photoresponse curve was measured by using a continuous-wave (CW) laser with 442 nm wavelength as the excited source and an oscilloscope as the data collector. The CW laser was chopped and modulated by a programmable module.

## 3. RESULTS AND DISCUSSION

The XRD pattern of the as-prepared  $\text{CsPbCl}_x\text{Br}_{3-x}$  crystal is shown in Fig. 1(a). Eight distinct peaks located at  $15.59^\circ$ ,  $15.7^\circ$ ,  $21.17^\circ$ ,  $31.38^\circ$ ,  $31.6^\circ$ ,  $35.37^\circ$ ,  $35.56^\circ$ , and  $38.7^\circ$  are detected. By comparing with the standard cards of  $\text{CsPbBr}_3$  (PDF #18-0364) and  $\text{CsPbCl}_3$  (PDF #18-0366), these peaks can be ascribed to the diffraction from the (001), (100), (101), (002), (200), (102), (201), and (112) facets of  $\text{CsPbCl}_x\text{Br}_{3-x}$ . The crystal constants of  $\text{CsPbBr}_3$  ( $5.827 \text{ \AA} \times 5.827 \text{ \AA} \times 5.891 \text{ \AA}$ ) are slightly larger than that of  $\text{CsPbCl}_3$  ( $5.584 \text{ \AA} \times 5.584 \text{ \AA} \times 5.623 \text{ \AA}$ ). Thus, compared with the standard XRD peaks of pure  $\text{CsPbBr}_3$ , these eight XRD peaks shift to the larger angle side, and compared with the XRD peaks of pure  $\text{CsPbCl}_3$ , they locate at the left angle side. Compared with the extremely high-crystal-quality hybrid perovskite  $\text{MAPbX}_3$  single crystal [23], the growth parameters including synthesized temperature, nucleation rate, reagent ratio, and additives need to be optimized in order to further improve the quality of  $\text{CsPbCl}_x\text{Br}_{3-x}$  crystal in the future. The optimized crystal quality can greatly improve the performance of the  $\text{CsPbCl}_x\text{Br}_{3-x}$  based optoelectronic devices. Figure 1(b) presents the Raman spectrum of the

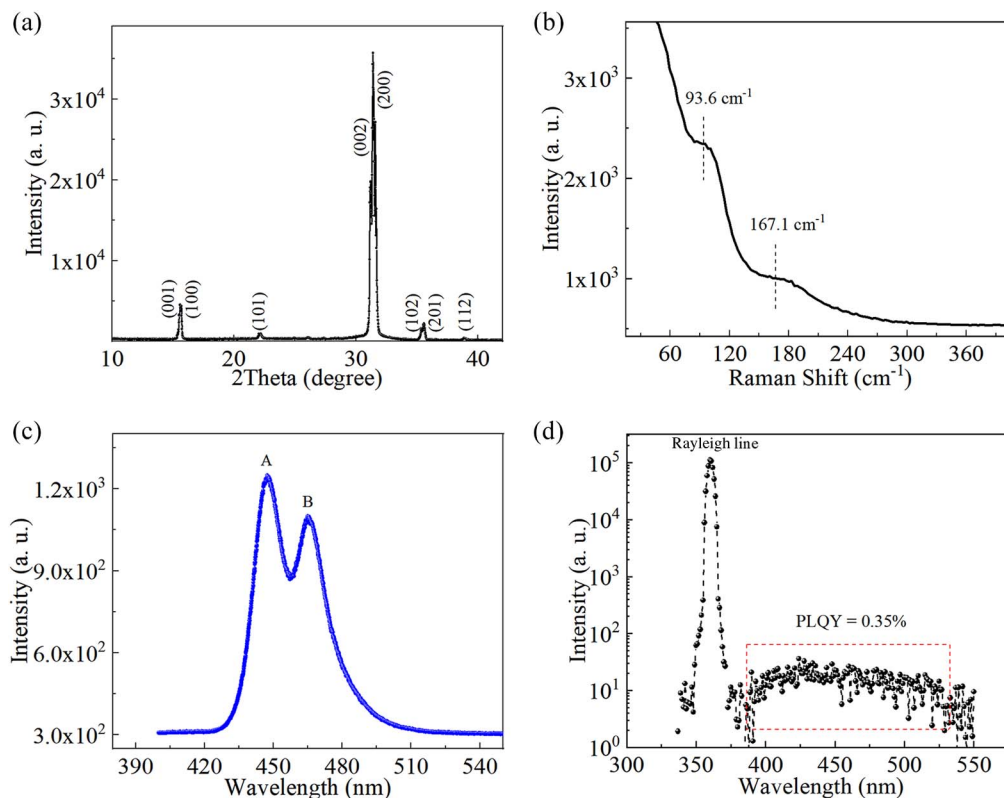


**Fig. 1.** The room temperature (a) XRD pattern, (b) Raman spectrum, (c) PL spectrum, and (d) PLQY of the as-synthesized  $\text{CsPbCl}_x\text{Br}_{3-x}$  crystal.

as-prepared  $\text{CsPbCl}_x\text{Br}_{3-x}$  sample, from which only two distinct Raman peaks centered at  $93.6\text{ cm}^{-1}$  and  $167.1\text{ cm}^{-1}$  are probed. According to previous Raman studies on  $\text{CsPbCl}_3$  [24,25], the first vibrational peak is relevant to the  $\text{Pb}(\text{Cl}_x\text{Br}_{1-x})_6$  octahedron and the second one is associated with the motion of  $\text{Cs}^+$  cations. Compared with the Raman peaks on  $\text{CsPbBr}_3$ , blue shifts can be determined owing to the substitution of a Br atom by a Cl atom [26,27]. The room temperature PL spectrum of the as-prepared  $\text{CsPbCl}_x\text{Br}_{3-x}$  crystal is exhibited in Fig. 1(c), from which a broad blue band emission is probed. Two distinct peaks denoted as peak A and peak B are detected; the former one is relevant to the bandgap emission and the latter one is induced by the donor defects. The optical images of the as-synthesized  $\text{CsPbCl}_x\text{Br}_{3-x}$  crystal are presented in Fig. 7 (Appendix A), suggesting a great number of crystal boundaries located within the surface of the sample. This will introduce a high concentration of surface defects, which supports the result from the PL measurement. It is worth noting that one key advantage in this work is the simple and low-cost equipment; only two beakers with different capacities are required, which makes the equipment easily upgraded. Then the  $\text{CsPbCl}_x\text{Br}_{3-x}$  crystals can be mass produced once the synthesized processes are mature. In addition, different from previous efforts on the high-quality perovskite crystal, defects and grain boundaries are intentionally introduced in order to study the defect tolerance of the optical pumping property, which will be discussed later. The bandgap of  $\text{CsPbCl}_x\text{Br}_{3-x}$  at room temperature is estimated as  $\sim 2.76\text{ eV}$  ( $\sim 448\text{ nm}$ ) by calculating the wavelength center of the bandgap emission, which

is  $\sim 0.45\text{ eV}$  larger than the bandgap of  $\text{CsPbBr}_3$  [28] and  $\sim 0.31\text{ eV}$  smaller than the bandgap of  $\text{CsPbCl}_3$  [29,30]. Quantum efficiency is one important parameter to measure the performance of emitters and the corresponding PLQY result is exhibited in Fig. 1(d). The PLQY of the sample is as low as 0.35%, which is quite similar to previous work reported by Gong *et al.* [31]; they only detect a low PLQY of 1% in a  $\text{CsPbBr}_3$  single crystal. Typically, different from  $\text{CsPbX}_3$  nanocrystals or quantum dots, bulk single crystal usually displays very low PLQY (typically  $\sim 1\%$  or even lower). One reason is owing to the presence of indirect tail states below the direct transition edge caused by Rashba splitting in bulk  $\text{CsPbBr}_3$  single crystal [32]. The other reason of the low PLQY is the high defect concentration in our  $\text{CsPbCl}_x\text{Br}_{3-x}$  crystal. Theoretically, the improvement of crystal quality is one effective strategy for improving the PLQY of  $\text{CsPbCl}_x\text{Br}_{3-x}$  crystal. A lower defect concentration can naturally decrease the nonradiative recombination centers, which brings the positive influence on the PLQY. Another strategy for improving the PLQY is decreasing the dimension of  $\text{CsPbCl}_x\text{Br}_{3-x}$  to quantum size (few nanometers). However, our aim is focusing on the large sized crystal; thus improving the crystal quality of  $\text{CsPbCl}_x\text{Br}_{3-x}$  crystals will be performed. Four strategies are considered in the future: (i) the synthesized temperature is enhanced from room temperature to  $60^\circ\text{C}$ – $80^\circ\text{C}$ , which provides sufficient thermal energy for the chemical reaction; (ii) a post-annealing process in the inert or halogen/lead atmosphere is considered; (iii) a specific organic molecule is selected and acts as the passivator of defects; (iv) the Bridgman method operated

at high temperature is considered for growing high-quality and large sized  $\text{CsPbCl}_x\text{Br}_{3-x}$  crystal, and then the sample is cut into the targeted size and polished. The high crystal quality will improve the PLQY of the crystal, and then decrease the threshold of the ASE. For photodetectors, undoubtedly, high crystal quality can lower the dark current of the device, and enhance the quantum efficiency and responsivity of the device. Especially, high crystal quality can naturally avoid the effect of trap states on the carrier dynamic, which contributes to the rapid response speed of a photodetector.

Figures 2(a)–2(d) present XPS spectra of Cs-3*d*, Pb-4*f*, Cl-2*p*, and Br-3*d* core electrons, in which C-1*s* peak (284.8 eV) is used as calibration. Apparently, all the orbitals can be well fitted with two standard Gaussian peaks, indicating the high-purity phase of  $\text{CsPbCl}_x\text{Br}_{3-x}$  crystal. The spin-orbital splittings (Cs-3*d*<sub>5/2</sub> and Cs-3*d*<sub>3/2</sub>; Pb-4*f*<sub>7/2</sub> and Pb-4*f*<sub>5/2</sub>; Cl-2*p*<sub>3/2</sub> and Cl-2*p*<sub>1/2</sub>; Br-3*d*<sub>5/2</sub> and Br-3*d*<sub>3/2</sub>) are calculated to be 14 eV, 4.87 eV, 1.6 eV, and 1.04 eV, agreeing well with the results from the standard XPS database. The energy band diagram is the key factor for semiconductor devices. The valence band scanning [Fig. 2(e)] and UPS measurement [Fig. 2(f)] are employed to determine the band structure of  $\text{CsPbCl}_x\text{Br}_{3-x}$ . Deriving from the cutoff and onset of the UPS spectrum, the work function of  $\text{CsPbCl}_x\text{Br}_{3-x}$  is calculated as ~3.8 eV and the Fermi energy level locates ~2.22 eV above the VBM. The UPS study aligns well with the Fermi energy level ( $E_F - E_{\text{VBM}} = \sim 2.3$  eV) confirmed by the valence band scanning spectrum. Therefore, the energy band diagram of  $\text{CsPbCl}_x\text{Br}_{3-x}$  can be summarized in Fig. 8 (Appendix A).

The energy difference between VBM and Pb-5*d*<sub>7/2</sub> orbital is 17 eV, and the Fermi energy level locates close to CBM.

Figure 3(a) displays the PL spectra under various excitation densities at room temperature, in which two distinct emissions (peak A and peak B) can be clearly observed. As further summarized in Fig. 3(b), the PL intensity at room temperature can be expressed by a power law ( $I \propto P^\alpha$ ), where  $I$  is the PL intensity,  $P$  is the excitation density, and  $\alpha$  is the exponent factor. The  $\alpha$  factors are calculated to be 0.34 (peak A) and 0.45 (peak B), which are smaller than one. Theoretically, when  $1 < \alpha < 2$ , excitonic recombination dominates; when  $\alpha$  is less than one, an impurity or defect (donor and acceptor) is involved in the transitions [33–36]. Thus, the small exponent factors indicate a large proportion of radiative recombination induced by defects. Theoretically, three factors including growth temperature, the ratio of the reaction solutes, and the growth rate (decided by the evaporation rate of methanol) have direct influence on the crystal quality. Low temperature (RT) cannot supply sufficient thermal energy for the migration of atoms, which will easily introduce defects in the crystal. Additionally, the methanol atmosphere can also affect the nucleation rate of  $\text{CsPbCl}_x\text{Br}_{3-x}$  crystals. The large diffusion rate of methanol atmosphere at a higher temperature will lead to the reduction of the growth time and also affect the crystal quality of the  $\text{CsPbCl}_x\text{Br}_{3-x}$  crystals. Nevertheless, in this work,  $\text{CsPbCl}_x\text{Br}_{3-x}$  crystals with a high defect concentration are intentionally synthesized, which is demonstrated by the low  $\alpha$  value. As previously mentioned, a high concentration of defects is probed in the as-synthesized  $\text{CsPbCl}_x\text{Br}_{3-x}$  crystal, agreeing well with the emission spectra

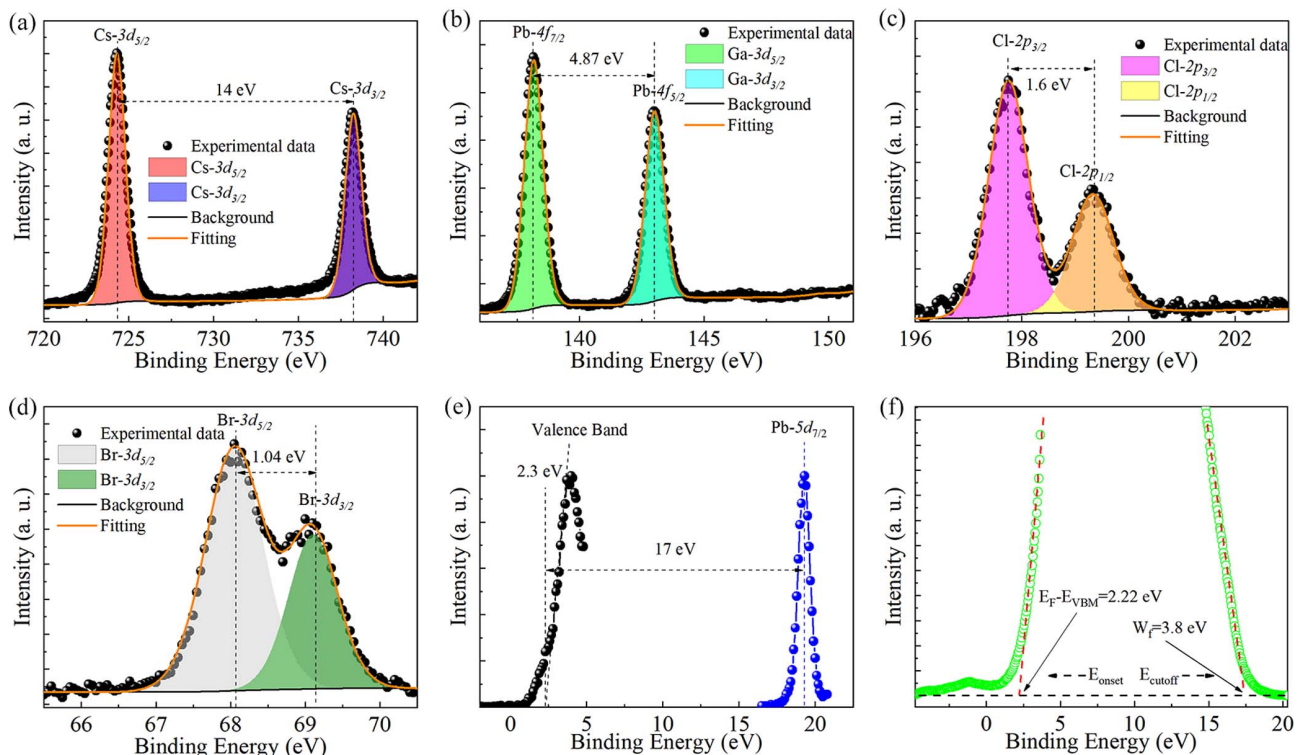


**Fig. 2.** The XPS spectra of (a) Cs-3*d*, (b) Pb-4*f*, (c) Cl-2*p*, and (d) Br-3*d* core electrons; (e) the valence band scanning spectrum of  $\text{CsPbCl}_x\text{Br}_{3-x}$  relative to the XPS spectrum of Pb-5*d*<sub>7/2</sub> core electron; (f) the UPS spectrum of  $\text{CsPbCl}_x\text{Br}_{3-x}$ .

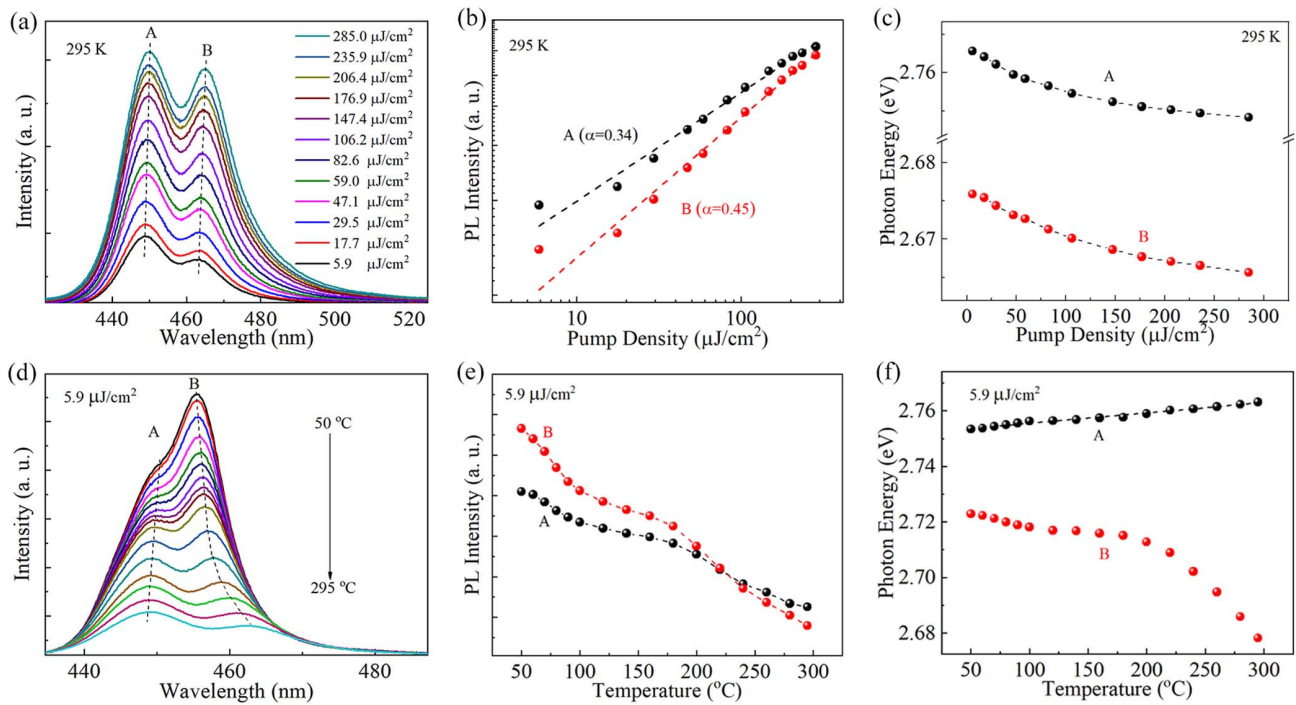


**Fig. 3.** (a) The room temperature PL spectra of the  $\text{CsPbCl}_x\text{Br}_{3-x}$  crystal under different excitation densities; (b) the relationship between the peak intensity and the excitation density; (c) the photon energy as a function of the excitation density; (d) temperature-dependent PL spectra of the  $\text{CsPbCl}_x\text{Br}_{3-x}$  crystal under the excitation density of  $5.9 \mu\text{J}/\text{cm}^2$ ; (e) the emission intensity as a function of the tested temperature; (f) temperature-dependent photon energies of peak A and peak B.

at room temperature. Figure 3(c) presents the excitation-intensity-dependent photon energies of peak A and peak B; both peak energies monotonically decrease with the increase of the excitation density. Typically, thermally induced lattice expansion can naturally reduce the bandgap of semiconductors [37,38]; thus the accumulated heat under higher excitation density is responsible for the red shift of the emission peaks at room temperature. Figure 3(d) shows the temperature-dependent PL spectra of the  $\text{CsPbCl}_x\text{Br}_{3-x}$  crystal at a low excitation ( $5.9 \mu\text{J}/\text{cm}^2$ ). With the increase of temperature, a blue shift of peak A and red shift of peak B are observed, which agrees well with previous reports [39,40]. Figure 3(e) summarizes the PL intensity at  $5.9 \mu\text{J}/\text{cm}^2$  as a function of the temperature. The PL intensity of peak B becomes larger than that of peak A when the temperature is below 220 K. Figure 3(f) presents the temperature-dependent photon energies of peak A and peak B under the excitation density of  $5.9 \mu\text{J}/\text{cm}^2$ . A slight blue shift on peak A and distinct red shift on peak B can be probed. The blue shift of peak A (bandgap emission) is unusual by comparing with conventional semiconductors like CdSe [41], ZnO [42], and GaN [43], but it is quite normal in perovskites [44–46]. A blue shift of  $\sim 10$  meV (peak A) is determined with temperature increasing from  $50^\circ\text{C}$  to  $295^\circ\text{C}$ . Generally, the temperature-dependent bandgap can be well fitted by a Varshni model [45,47]:

$$E_g(T) = E(0) - (\gamma \times T^2)/(\beta + T), \quad (1)$$

where  $E_g(T)$  and  $E(0)$  are the photon energies at  $T$  and  $0$  K;  $\gamma$  and  $\beta$  are shift parameters. The Varshni fit yields a  $\gamma$  parameter of  $-3.74 \times 10^{-5} \text{ K}^{-1}$ . The negative value indicates the slight blue

shift characteristic, and the  $\beta$  parameter at  $300$  K is corresponding to the Debye temperature. This behavior can be dominated by the bandgap renormalization effect in perovskite, which is completed by the thermal expansion and the interaction with phonons [48,49]. Normally, thermal expansion in perovskite materials will lead to the blue shift of the bandgap, while the interaction with phonons will induce the red shift of the bandgap [50,51]. Both volume dilation and excitation of the lattice vibration (phonon) are relevant to the temperature, which can produce the shifts in energy levels and then change the energy bandgap. The electron-phonon interaction can induce the shift of the valence band and conduction band, resulting in a quadratic variation of the energy gap at low temperature and a linear shift at high temperature [50]. The conduction band is estimated from the electron and the filled band should be decided by the hole with a negative sign in the effective mass. For perovskite materials, volume dilation has a higher effect on producing the temperature variation of the bandgap than the lattice vibrations. Therefore, a blue shift induced by thermal expansion dominates over the bandgap renormalization, thus leading to a blue shift of the bandgap as the temperature increases. Undoubtedly, the bandgap blue shift with the increase of temperature has been expected in a great number of perovskite materials.

Figure 4(a) exhibits the PL spectra of the as-grown  $\text{CsPbCl}_x\text{Br}_{3-x}$  crystal under different pumping densities ( $5.9 \mu\text{J}/\text{cm}^2$  to  $235.9 \mu\text{J}/\text{cm}^2$ ) at  $50$  K. Broad spontaneous emissions ranging from  $435$  nm to  $480$  nm dominate as the pumping density is below the threshold ( $106 \mu\text{J}/\text{cm}^2$ ). As the pumping density reaches the threshold, the intensity of

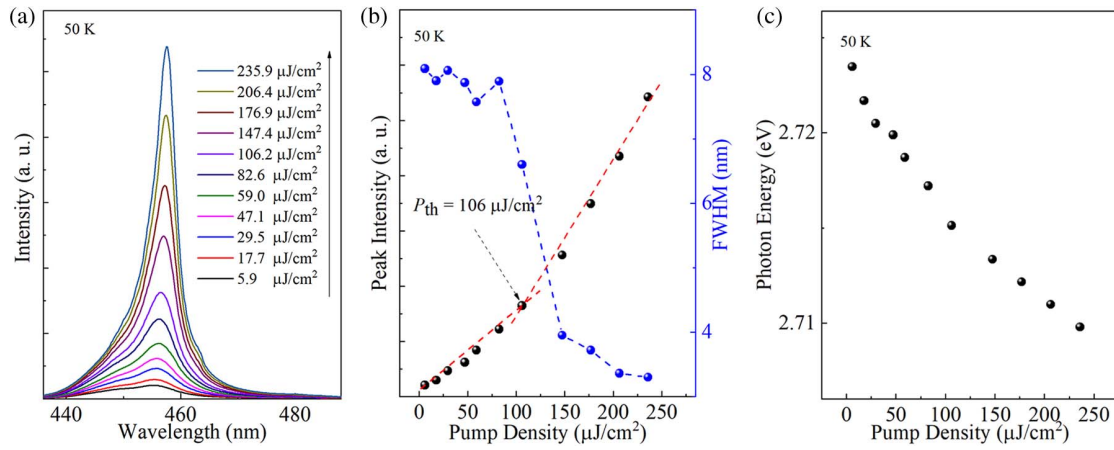


**Fig. 4.** (a) The ASE from the  $\text{CsPbCl}_x\text{Br}_{3-x}$  crystal under various pumping densities; (b) the PL intensity (black) and FWHM (blue) as a function of the pumping density; (c) the ASE peak energy as a function of the pumping density.

the PL peak centered at  $\sim 456$  nm is greatly enhanced. As the pumping density is further enhanced, the PL intensity increases with a nonlinear slope [Fig. 4(b)]. In addition, the FWHM of the PL spectrum sharply decreases from  $\sim 8.1$  nm to  $\sim 3.6$  nm as the emission transits from spontaneous emission to ASE. This ASE behavior is highly accordant with exciton-exciton inelastic scattering, which is also observed in the  $\text{CsPbBr}_3$  film [51]. Even though our sample exhibits a high-defect appearance, ASE still can be realized at a relatively low pumping density, further proving the high defect tolerance of the emerging perovskite. However, compared with the ASE in  $\text{CsPbBr}_3$  realized at room temperature [10], the ASE of  $\text{CsPbCl}_x\text{Br}_{3-x}$  crystal is probed at low temperature. Typically, most intrinsic defects in  $\text{CsPbBr}_3$  with low formation energies such as vacancies ( $V_{\text{Cs}}$ ,  $V_{\text{Pb}}$ , and  $V_{\text{Br}}$ ) induce shallow defect levels [52]. However, the defect energy levels of halide vacancies ( $V_{\text{Cl}}$ ) are relatively deep in  $\text{CsPbCl}_3$  [53]. Thus, the PLQY of  $\text{CsPbCl}_3$  is normally lower than that of  $\text{CsPbBr}_3$  [54]. In this work, the ASE can still be observed in  $\text{CsPbCl}_x\text{Br}_{3-x}$  crystal, which may be ascribed to the following: (i) in the alloy system ( $\text{CsPbCl}_x\text{Br}_{3-x}$ ), the defect level of  $V_{\text{Cl}}$  is deeper than that in  $\text{CsPbBr}_3$  but shallower than that in  $\text{CsPbCl}_3$ ; (ii) compared with  $\text{CsPbCl}_3$ , the electronic state density of the defect levels ( $V_{\text{Cl}}$ ) in  $\text{CsPbCl}_x\text{Br}_{3-x}$  is relatively low, indicating the less non-radiative recombination sites; (iii) the measured temperature is 50 K, which can effectively suppress the non-radiative recombination. Figure 4(c) displays the pump-density-dependent

peak energy at 50 K. Apparently, a red shift is probed as the pumping density increases, which is similar to previous reports on  $\text{CsPbBr}_3$  [48,55,56]. Typically, the ASE emission peak energy  $E$  is relevant to the exciton density and temperature, which can be expressed as [57]

$$E = E_{\text{ex}} - E_{\text{b}} \left( 1 - \frac{1}{n^2} \right) - 3 \delta k_{\text{b}} T, \quad n = 2, 3, 4, \dots, \quad (2)$$

where  $E_{\text{ex}}$  is the free exciton energy,  $E_{\text{b}}$  is the exciton binding energy,  $n$  is the exciton level,  $\delta$  is a constant between zero and one,  $k_{\text{b}}$  is the Boltzmann constant, and  $T$  is the effective temperature. With the increase of the pumping density, the excitons are pumped to the lower levels at the polariton curve ( $n = 2, 3, 4, 5, 6, \dots$ ); thus  $E_{\text{b}}(1 - \frac{1}{n^2})$  increases. At the same time, the thermal effect induced by the optical pumping simultaneously leads to the enhancement of effective temperature. According to Eq. (2), a red shift of ASE with the increase of pumping density is naturally expected in  $\text{CsPbCl}_x\text{Br}_{3-x}$  crystals. Table 1 concludes the comparison of the ASE values on  $\text{CsPbX}_3$  perovskites. Most reports are concerning the low-dimensional structures like quantum dots, nanocrystals, and microplates, which are much easier in the realization of ASE because of the quantum size effect. However, in this work, the realization of ASE in larger sized (0.5–2 mm) perovskite crystals will give rise to the potential application in a crystal laser by using  $\text{CsPbCl}_x\text{Br}_{3-x}$  as the gain medium.

**Table 1.** Comparison of the ASE Parameters Reported for  $\text{CsPbX}_3$  Perovskites

Morphology	Sample Size	Emission Wavelength	Threshold	FWHM	Growth Temperature	Ref.
$\text{CsPbCl}_x\text{Br}_{3-x}$ single crystal	0.5–2 mm	$\sim 456$ nm	106 $\mu\text{J}/\text{cm}^2$	3.6 nm	RT	This work
$\text{CsPbCl}_x\text{Br}_{3-x}$ quantum dots	10.4–11.5 nm	468, 498 nm	43–45 $\mu\text{J}/\text{cm}^2$	6.71, 6.15 nm	-	[11]
$\text{CsPbCl}_x\text{Br}_{3-x}$ quantum dots	12 $\pm$ 1 nm	440, 470, 506 nm	20–50 $\mu\text{J}/\text{cm}^2$	5.7–8.5 nm	190°C	[12]
$\text{CsPbCl}_x\text{Br}_{3-x}$ nanofilm	-	495 nm	56.1 $\mu\text{J}/\text{cm}^2$	$\sim 5$ nm	25°C–200°C	[13]
$\text{CsPbBr}_3$ single crystal	650–700 $\mu\text{m}$	538 nm	1.38 mJ/cm <sup>2</sup>	$\sim 4$ nm	800°C	[14]
$\text{CsPbBr}_3$ nanoparticle	$\sim 12$ nm	$\sim 528$ nm	1.2 $\mu\text{J}/\text{cm}^2$	$\sim 4$ nm	185°C	[58]
$\text{CsPbBr}_3$ nanocrystal	$\sim 8.67$ nm	526.7 nm	2.55 mJ/cm <sup>2</sup>	7.8 nm	180°C	[59]
$\text{CsPbBr}_3$ quantum dots	5–20 nm	$\sim 538$ nm	320 $\mu\text{J}/\text{cm}^2$	$\sim 4$ nm	440°C–530°C	[60]
$\text{CsPbBr}_3$ microplate	0.77–6.5 $\mu\text{m}$	537 nm	300 $\mu\text{J}/\text{cm}^2$	$\sim 1$ nm	-	[61]

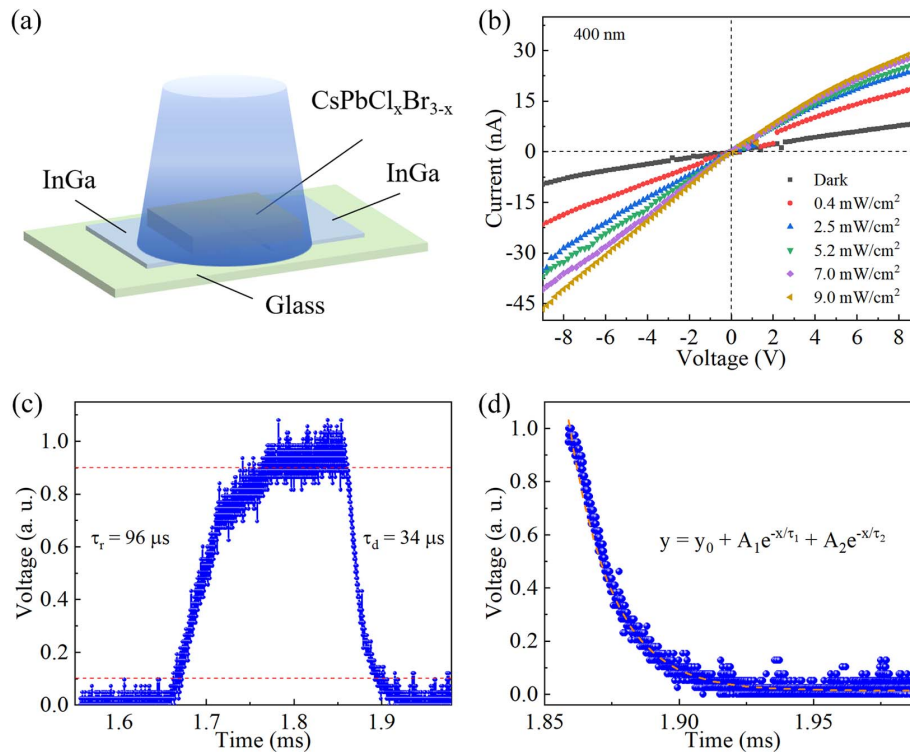


**Fig. 5.** (a) The schematic diagram of the  $\text{CsPbCl}_x\text{Br}_{3-x}$  photodetector; (b) the  $I$ - $V$  curves of the  $\text{CsPbCl}_x\text{Br}_{3-x}$  photodetector under dark and 400 nm light illumination; (c) the fast response  $V$ - $t$  measurement and (d) the fitting of the decay trace.

The schematic diagram of the  $\text{CsPbCl}_x\text{Br}_{3-x}$  photodetector is presented in Fig. 5(a), from which InGa metal is employed as the bottom electrodes. Figure 5(b) shows the  $I$ - $V$  curves of the photodetector under dark and illumination by 400 nm light with different intensities. The nearly linear relationship between voltage and dark current indicates the Ohmic contact between InGa and  $\text{CsPbCl}_x\text{Br}_{3-x}$ . According to previous UPS measurement, the work function of  $\text{CsPbCl}_x\text{Br}_{3-x}$  is determined to be  $\sim 3.8$  eV, which is close to that of the InGa electrode ( $\sim 4.1$  eV) [62]. Combining the surface defect states in the sample, the Ohmic contact property can be naturally expected between the metal and semiconductor. Under irradiation of the 400 nm light [Fig. 5(b)], the photocurrent prominently increases, and it is enhanced with the increase of the light intensity. The response speed is also an important parameter for the photodetector, which represents its signal tracking ability. As presented in Fig. 5(c), the response curve is asymmetrical with a rise time of  $96 \mu\text{s}$  and a decay time of  $34 \mu\text{s}$ , which reveals a fast response performance. The 3 dB bandwidth can be further calculated as 140 kHz. Additionally, the decay of the response curve can be well fitted with a second order exponential equation [63]:

$$y = y_0 + A_1 e^{-\tau/\tau_1} + A_2 e^{-\tau/\tau_2}, \quad (3)$$

where  $y_0$  is the maximum voltage,  $A_1$  and  $A_2$  are fitting constants, and  $\tau_1$  and  $\tau_2$  are the first order decay time and second order decay time. As exhibited in Fig. 5(d),  $\tau_1$  and  $\tau_2$  are well fitted as  $25.6 \mu\text{s}$  and  $31.3 \mu\text{s}$ , which means two physical processes are responsible for the recovery time once the illumination is turned off. Nevertheless, both processes show fast response

behavior. As discussed above, the defect energy level of  $V_{\text{Br}}$  is shallow in  $\text{CsPbBr}_3$  while that of  $V_{\text{Cl}}$  is relatively deep in  $\text{CsPbCl}_3$ ; the deep level of  $V_{\text{Cl}}$  may bring a negative effect on the recovery time of the photodetector. However, in the  $\text{CsPbCl}_x\text{Br}_{3-x}$  crystal, the deep-level property of  $V_{\text{Cl}}$  will be partly suppressed. Therefore, the fast response speed of the device can still be obtained in the low-quality  $\text{CsPbCl}_x\text{Br}_{3-x}$  crystals. Typically, three factors including the RC time constant, the transit time, and the excess life time of the trap carriers are responsible for the decay trace [64]. Herein, the RC time constant is originated from the large capacitance from the PN junction or Schottky junction, which can be ruled out in our photoconductive device. The transit time is determined by the space of two electrodes, the applied voltage, and the carrier mobility [65]. According to the parameters of the device, the transit time is estimated as  $27.9 \mu\text{s}$ , which may be the most possible reason for the  $\tau_1$  value. Additionally, the trapped carriers induced by the defects in the surface or the grain boundaries will lead to the excess life time as the incident light is turned off; this mean life time can be indexed to the  $\tau_2$  time constant. Therefore, the decay time of the photodetector is contributed by the transit time and the excess life time of the trap carriers induced by defects.

The energy band diagram of the symmetric structure InGa/ $\text{CsPbCl}_x\text{Br}_{3-x}$ /InGa photodetector can be observed in Fig. 6(a). The Fermi energy level locates  $\sim 0.54$  eV below the CBM, implying the  $n$ -type conductivity of the perovskite. The energy band offset between the work functions of InGa and  $\text{CsPbCl}_x\text{Br}_{3-x}$  is as small as  $\sim 0.3$  eV. Considering the

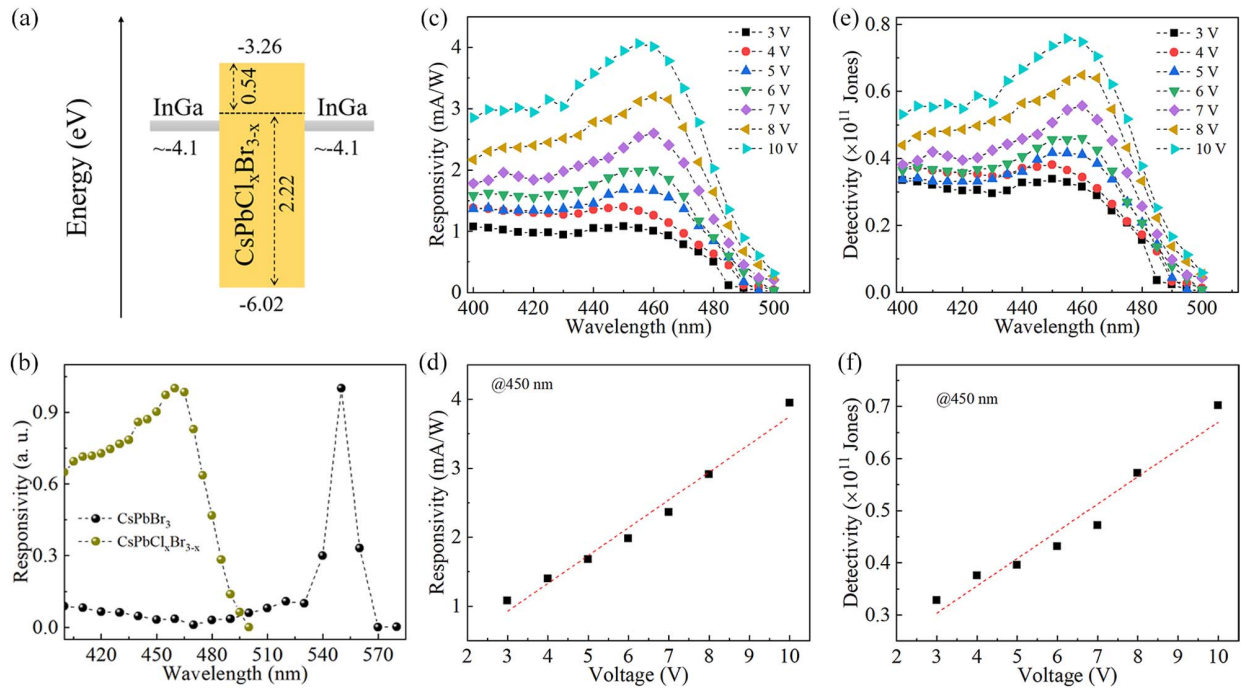


**Fig. 6.** (a) The energy band diagram of the  $\text{InGa}/\text{CsPbCl}_x\text{Br}_{3-x}/\text{InGa}$  device versus vacuum energy level; (b) the response spectra of  $\text{CsPbCl}_x\text{Br}_{3-x}$  and  $\text{CsPbBr}_3$  photodetectors; (c) the wavelength-dependent responsivity of the  $\text{CsPbCl}_x\text{Br}_{3-x}$  photodetector under different bias voltages; (d) the responsivity at  $450$  nm as a linear function of the applied voltage; (e) the wavelength-dependent detectivity of the  $\text{CsPbCl}_x\text{Br}_{3-x}$  photodetector under different bias voltages; (f) the detectivity at  $450$  nm as a linear function of the applied voltage.

energy level broadening and surface state or defect on the surface of  $\text{CsPbCl}_x\text{Br}_{3-x}$ , the shallow barrier can be easily ignored. So, the Ohmic contact property is probed in Fig. 5(b). Figure 6(b) exhibits the comparison of response spectra between the  $\text{CsPbBr}_3$  photodetector and the  $\text{CsPbCl}_x\text{Br}_{3-x}$  photodetector. Apparently, substitution of Br by Cl can widen the bandgap of  $\text{CsPbBr}_3$ ; the response spectrum range of  $\text{CsPbCl}_x\text{Br}_{3-x}$  is correspondingly modulated toward the shorter wavelength region. Additionally, the  $\text{CsPbBr}_3$  single crystal normally reveals a narrow band ( $\sim 30$  nm) response characteristic, which is explained by the CCN mechanism [21]. Nevertheless, this phenomenon is not probed in the  $\text{CsPbCl}_x\text{Br}_{3-x}$  photodetector, which harvests broad spectra from UV to the blue band. This may be ascribed to the change of band structure as Br is substituted by Cl. The responsivity under different applied voltages is provided in Fig. 6(c) and the responsivity illuminated by  $450$  nm light is extracted in Fig. 6(d). At  $10$  V, the responsivity at  $450$  nm is calculated as  $3.95$  mA/W and it linearly depends on the working voltage. Correspondingly, the detectivities of the device under different voltages are further studied and displayed in Figs. 6(e) and 6(f). Similarly, the voltage-dependent detectivity also follows the linear tendency, and the detectivity at  $10$  V ( $@450$  nm) is  $7 \times 10^{10}$  Jones. The linear dependency indicates the carrier extracted efficiency is linearly depending on the external bias voltage. Figure 9 (Appendix A) exhibits the external quantum efficiency (EQE) of the device at different bias voltages. At  $10$  V, the EQE at  $450$  nm is as small as  $\sim 1.1\%$ , indicating the low collection efficiency of the photo-generated carriers. In addition, the dark current of the device is relatively

high and the light-dark current ratio is low. As mentioned above, a high defect concentration and numerous grain boundaries are probed on the as-synthesized  $\text{CsPbCl}_x\text{Br}_{3-x}$  crystals. The defects in the crystal normally act as donors, which leads to the high background carrier concentration, and the scattering and non-radiative recombination induced by the defects and grain boundaries significantly reduce the EQE of the photodetector. Therefore, the crystal quality of the  $\text{CsPbCl}_x\text{Br}_{3-x}$  crystal needs to be further improved in order to enhance the photodetection performance. Synthesized parameters such as growth temperature, reagent ratio, and nucleation rate should be carefully considered. During the photoelectronic measurement, the device is exposed in air conditioning with RH of  $\sim 57\%$ . The photodetector  $\text{CsPbCl}_x\text{Br}_{3-x}$  shows good stability at the air atmosphere (room temperature, RH  $< \sim 57\%$ ) and the photoresponse performance can be well maintained for over 6 months. However, once the RH of the environment is  $> 60\%$ , the photocurrent of the device slowly attenuates because of the hydrolysis of the perovskite. Owing to the intrinsic ionic feature, the interaction between perovskite and water is the main reason of the degradation of the perovskite devices [66], which is named as the well known instability in halide perovskites. For example, though a capping layer is introduced for isolating the water, the power conversion efficiency of the perovskite is reduced to  $23.5\%$  at  $80\%$  RH, which is lower than that at  $20\%$ – $60\%$  RH [67]. In addition, the oxidation of the surface is another unfavorable factor that can also degrade the photoelectronic performance of the perovskite devices, while the oxidation process typically needs an extremely long time at room temperature in air atmosphere.

Therefore, water is the most unstable factor for perovskite devices. Industrial grade packaging with resin or a polymer layer can effectively protect the perovskite active layer and prolong the life time of the perovskite devices.

#### 4. CONCLUSIONS

Herein, the highly defect tolerant  $\text{CsPbCl}_x\text{Br}_{3-x}$  crystals are synthesized via a room temperature anti-solvent precipitation process. Spontaneous and amplified spontaneous emissions are both studied under different temperatures and pumping densities. The blue band ASE emissions centered at  $\sim 456$  nm are probed with a relatively low threshold of  $106 \mu\text{J}/\text{cm}^2$  at 50 K. Though the as-prepared  $\text{CsPbCl}_x\text{Br}_{3-x}$  crystal reveals a high defect concentration, ASE is still realized between the competition of radiative recombination and defect-related nonradiative recombination, indicating the highly defect tolerant  $\text{CsPbCl}_x\text{Br}_{3-x}$  as a promising material for optoelectronic devices. Furthermore, an MSM structure  $\text{CsPbCl}_x\text{Br}_{3-x}$  photodetector is prepared and shows a fast response performance with response speeds of  $96 \mu\text{s}$  (rise time) and  $34 \mu\text{s}$  (decay time). Our findings enhance the understanding of the light amplification properties in all inor-

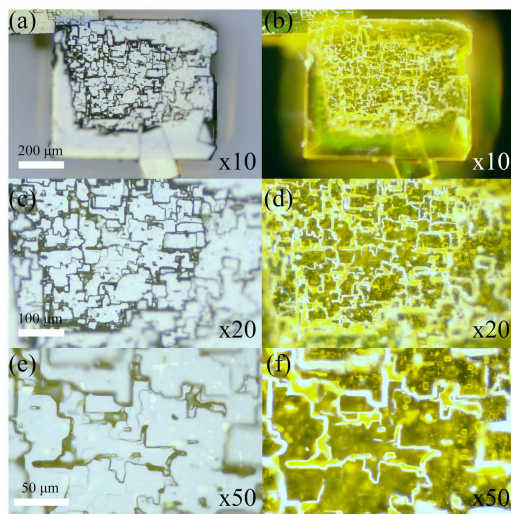


**Fig. 7.** The bright field (a), (c), (e) and dark field (b), (d), (f) optical images of the  $\text{CsPbCl}_x\text{Br}_{3-x}$  crystal at different magnifications.

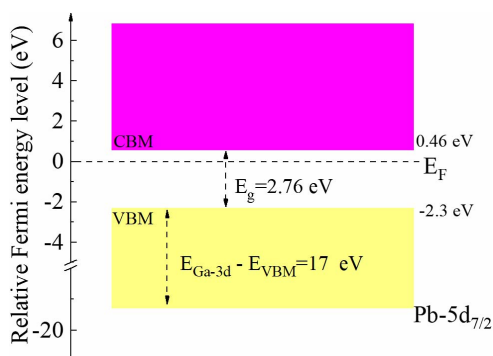


**Fig. 8.** The energy band diagram of the  $\text{CsPbCl}_x\text{Br}_{3-x}$  crystal.

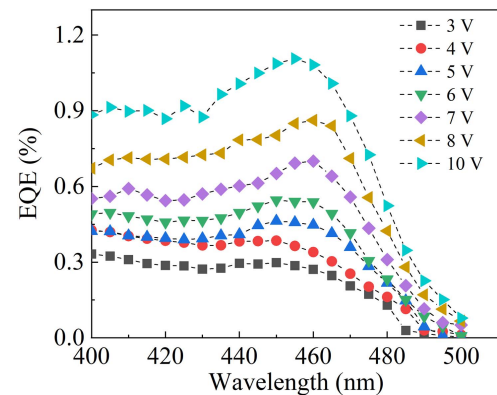


**Fig. 9.** The external quantum efficiency (EQE) of the  $\text{CsPbCl}_x\text{Br}_{3-x}$  photodetector.

ganic perovskite, as well as the fabrication of a next generation high-performance photodetector.

#### APPENDIX A

Optical images and the energy band diagram of the  $\text{CsPbCl}_x\text{Br}_{3-x}$  crystal are shown in Figs. 7 and 8, respectively. Figure 9 illustrates the external quantum efficiency of the  $\text{CsPbCl}_x\text{Br}_{3-x}$  photodetector.

**Funding.** National Natural Science Foundation of China (52172149); Youth S&T Talent Support Programme of Guangdong Provincial Association for Science and Technology (SKXRC202405); Guangdong Provincial Key Laboratory Project (High-Performance Integrated Circuits and Systems Laboratory, 2023KSYS003).

**Acknowledgment.** The XRD, PLQY, and XPS data were obtained using the equipment maintained by Dongguan University of Technology Analytical and Testing Center. The authors thank Dr. F. Yi for the helpful discussion on this manuscript.

**Disclosures.** The authors declare no competing financial interests.

**Data Availability.** The data that support the findings of this study are available from the corresponding author upon reasonable request.

#### REFERENCES

1. X. B. Wang, X. Y. Zhang, H. Liu, *et al.*, "Self-assembling nanoarchitectonics of low dimensional semiconductors for circularly polarized luminescence," *J. Materiomics* **9**, 683–700 (2023).
2. Y. L. Lia, H. X. Sun, Z. Lia, *et al.*, "Electrospun perovskite nano-network for flexible, near-room temperature, environmentally friendly and ultrastable light regulation," *J. Mater. Sci. Technol.* **130**, 35–43 (2022).
3. M. V. Kovalenko, L. Protesescu, and M. I. Bodnarchuk, "Properties and potential optoelectronic applications of lead halide perovskite nanocrystals," *Science* **358**, 745–750 (2017).
4. C. Y. Wu, Y. X. Le, L. Y. Liang, *et al.*, "Non-ultrawide bandgap  $\text{CsPbBr}_3$  nanosheet for sensitive deep ultraviolet photodetection," *J. Mater. Sci. Technol.* **159**, 251–257 (2023).

5. X. X. He, P. Liu, H. H. Zhang, *et al.*, "Patterning multicolored microdisk laser arrays of cesium lead halide perovskite," *Adv. Mater.* **29**, 1604510 (2017).
6. B. Liu, Y. Q. Wang, Y. J. Wu, *et al.*, "Novel broad spectral response perovskite solar cells: a review of the current status and advanced strategies for breaking the theoretical limit efficiency," *J. Mater. Sci. Technol.* **140**, 33–57 (2023).
7. Q. A. Akkerman, V. D'Innocenzo, S. Accornero, *et al.*, "Tuning the optical properties of cesium lead halide perovskite nanocrystals by anion exchange reactions," *J. Am. Chem. Soc.* **137**, 10276–10281 (2015).
8. Y. P. Huang, Z. W. Lai, J. W. Jin, *et al.*, "Ultrasensitive temperature sensing based on ligand-free alloyed CsPbCl<sub>1-x</sub>Br<sub>3-x</sub> perovskite nanocrystals confined in hollow mesoporous silica with high density of halide vacancies," *Small* **17**, 2103425 (2021).
9. J. M. Pina, D. H. Parmar, G. Bappi, *et al.*, "Deep-blue perovskite single-mode lasing through efficient vapor-assisted chlorination," *Adv. Mater.* **33**, 2006697 (2021).
10. L. X. Su, "Room temperature amplified spontaneous emissions in a sub-centimeter sized CsPbBr<sub>3</sub> bulk single crystal," *Opt. Express* **31**, 39020–39029 (2023).
11. S. M. H. Qaid, H. M. Ghaithan, B. A. Al-Asbahi, *et al.*, "Tuning of amplified spontaneous emission wavelength for green and blue light emission through the tunable composition of CsPb(Br<sub>1-x</sub>Cl<sub>x</sub>)<sub>3</sub> inorganic perovskite quantum dots," *J. Phys. Chem. C* **125**, 9441–9452 (2021).
12. H. H. Zhang, J. N. Yao, and H. B. Fu, "Patterning rainbow like amplified spontaneous emission arrays for full-color CsPbX<sub>3</sub> quantum dot film displays," *Chem. Mater.* **32**, 9602–9608 (2020).
13. N. Liu, H. Y. Luo, X. Y. Wei, *et al.*, "Linearly manipulating color emission via anion exchange technology for high performance amplified spontaneous emission of perovskites," *Adv. Mater.* **36**, 2308672 (2024).
14. D. Kim, H. Ryu, S. Y. Lim, *et al.*, "On the origin of room-temperature amplified spontaneous emission in CsPbBr<sub>3</sub> single crystals," *Chem. Mater.* **33**, 7185–7193 (2021).
15. C. Y. Zhao, W. M. Tian, J. X. Liu, *et al.*, "Stable two-photon pumped amplified spontaneous emission from millimeter-sized CsPbBr<sub>3</sub> single crystals," *J. Phys. Chem. Lett.* **10**, 2357–2362 (2019).
16. L. X. Su, T. F. Li, and Y. Zhu, "A vertical CsPbBr<sub>3</sub>/ZnO heterojunction for photo-sensing lights from UV to green band," *Opt. Express* **30**, 23330–23340 (2022).
17. C. Fu, Z.-Y. Li, J. Wang, *et al.*, "A simple-structured perovskite wavelength sensor for full-color imaging," *Nano Lett.* **23**, 533–540 (2023).
18. Y. Li, Z. F. Shi, L. Z. Lei, *et al.*, "Highly stable perovskite photodetector based on vapor-processed micrometer-scale CsPbBr<sub>3</sub> microplatelets," *Chem. Mater.* **30**, 6744–6755 (2018).
19. J. Z. Song, Q. Z. Cui, J. H. Li, *et al.*, "Ultralarge all-inorganic perovskite bulk single crystal for high-performance visible-infrared dual-modal photodetectors," *Adv. Opt. Mater.* **5**, 1700157 (2017).
20. Y. Zhang, S. Y. Li, W. Yang, *et al.*, "Millimeter-sized single-crystal CsPbBr<sub>3</sub>/CuI heterojunction for high-performance self-powered photodetector," *J. Phys. Chem. Lett.* **10**, 2400–2407 (2019).
21. F. M. Guo, J. Wang, Y. Li, *et al.*, "Poststriping fabrication and self-driven narrowband photoresponse of large-grain, phase-pure CsPbBr<sub>3</sub> films," *Sol. RRL* **6**, 2200828 (2022).
22. H. R. Sun, L. X. Su, Q. Zeng, *et al.*, "Kilogram-scale high-yield production of PbI<sub>2</sub> microcrystals for optimized photodetectors," *J. Mater. Chem. C* **12**, 6433–6442 (2024).
23. S. Mahato, M. T. Szwajkowska, S. Singh, *et al.*, "Surface-engineered methylammonium lead bromide single crystals: a platform for fluorescent security tags and photodetector applications," *Adv. Opt. Mater.* **12**, 2302257 (2024).
24. M. L. Liao, B. B. Shan, and M. Li, "In situ Raman spectroscopic studies of the thermal stability of all-inorganic cesium lead halide (CsPbX<sub>3</sub>, X = Cl, Br, I) perovskite nanocrystals," *J. Phys. Chem. Lett.* **10**, 1217–1225 (2019).
25. D. M. Calistru, L. Mihut, S. Lefrant, *et al.*, "Identification of the symmetry of phonon modes in CsPbCl<sub>3</sub> in phase IV by Raman and resonance-Raman scattering," *J. Appl. Phys.* **82**, 5391–5395 (1997).
26. L. X. Su, "Room temperature growth of CsPbBr<sub>3</sub> single crystal for asymmetric MSM structure photodetector," *J. Mater. Sci. Technol.* **187**, 113–122 (2024).
27. L. X. Su, "Growth of a sub-centimeter-sized CsPbBr<sub>3</sub> bulk single crystal using an anti-solvent precipitation method," *Symmetry* **16**, 332 (2024).
28. L. X. Su, Y. Zhang, and J. Xie, "All-inorganic CsPbBr<sub>3</sub>/GaN heterostructure for near UV to green band photodetector," *J. Mater. Chem. C* **10**, 1349–1356 (2022).
29. M. Baranowski, P. Plochocka, R. Su, *et al.*, "Exciton binding energy and effective mass of CsPbCl<sub>3</sub>: a magneto-optical study," *Photon. Res.* **8**, A50–A55 (2020).
30. F. Xu, H. M. Wei, Y. Q. Wu, *et al.*, "Nonmonotonic temperature-dependent bandgap change of CsPbCl<sub>3</sub> films induced by optical phonon scattering," *J. Lumin.* **257**, 119736 (2023).
31. J. B. Gong, H. X. Zhong, C. Gao, *et al.*, "Pressure-induced indirect-direct bandgap transition of CsPbBr<sub>3</sub> single crystal and its effect on photoluminescence quantum yield," *Adv. Sci.* **9**, 2201554 (2022).
32. B. Wu, H. F. Yuan, Q. Xu, *et al.*, "Indirect tail states formation by thermal-induced polar fluctuations in halide perovskites," *Nat. Commun.* **10**, 484 (2019).
33. S. Jin, Y. L. Zheng, and A. Z. Li, "Characterization of photoluminescence intensity and efficiency of free excitons in semiconductor quantum well structures," *J. Appl. Phys.* **82**, 3870–3873 (1997).
34. D. E. Cooper, J. Bajaj, and P. R. Newmann, "Photoluminescence spectroscopy of excitons for evaluation of high-quality CdTe crystals," *J. Cryst. Growth* **86**, 544–551 (1988).
35. Z. C. Feng, A. Mascarenhas, and W. J. Choyke, "Low temperature photoluminescence spectra of (001) CdTe films grown by molecular beam epitaxy at different substrate temperatures," *J. Lumin.* **35**, 329–341 (1986).
36. L. Bergman, X. B. Chen, J. L. Morrison, *et al.*, "Photoluminescence dynamics in ensembles of wide-band-gap nanocrystallites and powders," *J. Appl. Phys.* **96**, 675–682 (2004).
37. H. P. He, H. P. Tang, Z. Z. Ye, *et al.*, "Temperature-dependent photoluminescence of quasialigned Al-doped ZnO nanorods," *Appl. Phys. Lett.* **90**, 023104 (2007).
38. C. X. Shan, Z. Liu, and S. K. Hark, "Temperature dependent photoluminescence study on phosphorus doped ZnO nanowires," *Appl. Phys. Lett.* **92**, 073103 (2008).
39. S. H. Yu, J. Xu, X. Y. Shang, *et al.*, "Unusual temperature dependence of bandgap in 2D inorganic lead-halide perovskite nanoplatelets," *Adv. Sci.* **8**, 2100084 (2021).
40. K. Mukhuti, A. Mandal, B. Roy, *et al.*, "Carrier thermalization and zero-point bandgap renormalization in halide perovskites from the Urbach tails of the emission spectrum," *Appl. Phys. Lett.* **121**, 182104 (2022).
41. S. Bose, S. Shendre, Z. G. Song, *et al.*, "Temperature-dependent optoelectronic properties of quasi-2D colloidal cadmium selenide nanoplatelets," *Nanoscale* **9**, 6595–6605 (2017).
42. R. Chen, Q.-L. Ye, T. C. He, *et al.*, "Uniaxial tensile strain and exciton-phonon coupling in bent ZnO nanowires," *Appl. Phys. Lett.* **98**, 241916 (2011).
43. A. J. Fischer, W. Shan, J. J. Song, *et al.*, "Temperature-dependent absorption measurements of excitons in GaN epilayers," *Appl. Phys. Lett.* **71**, 1981–1983 (1997).
44. B. T. Diroll, G. Nedelcu, M. V. Kovalenko, *et al.*, "High-temperature photoluminescence of CsPbX<sub>3</sub> (X = Cl, Br, I) nanocrystals," *Adv. Funct. Mater.* **27**, 1606750 (2017).
45. J. Li, X. Yuan, P. Jing, *et al.*, "Temperature-dependent photoluminescence of inorganic perovskite nanocrystal films," *RSC Adv.* **6**, 78311–78316 (2016).
46. M. I. Dar, G. Jacopin, S. Meloni, *et al.*, "Origin of unusual bandgap shift and dual emission in organic-inorganic lead halide perovskites," *Sci. Adv.* **2**, e1601156 (2016).
47. Y. P. Varshni, "Temperature dependence of the energy gap in semiconductors," *Physica* **34**, 149–154 (1967).
48. J. Bardeen and W. Shockley, "Deformation potentials and mobilities in non-polar crystals," *Phys. Rev.* **80**, 72–80 (1950).
49. H. Y. Fan, "Temperature dependence of the energy gap in monatomic semiconductors," *Phys. Rev.* **78**, 808–809 (1950).

50. B. Liu, R. Chen, X. L. Xu, *et al.*, "Exciton-related photoluminescence and lasing in CdS nanobelts," *J. Phys. Chem. C* **115**, 12826 (2011).
51. Y. Q. Shi, R. X. Li, G. X. Yin, *et al.*, "Laser-induced secondary crystallization of CsPbBr<sub>3</sub> perovskite film for robust and low threshold amplified spontaneous emission," *Adv. Funct. Mater.* **32**, 2207206 (2022).
52. J. Kang and L. W. Wang, "High defect tolerance in lead halide perovskite CsPbBr<sub>3</sub>," *J. Phys. Chem. Lett.* **8**, 489–493 (2017).
53. D. P. Nenon, K. Pressler, J. Kang, *et al.*, "Design principles for trap-free CsPbX<sub>3</sub> nanocrystals: enumerating and eliminating surface halide vacancies with softer Lewis bases," *J. Am. Chem. Soc.* **140**, 17760–17772 (2018).
54. G. H. Ahmed, J. K. El-Demellawi, J. Yin, *et al.*, "Giant photoluminescence enhancement in CsPbCl<sub>3</sub> perovskite nanocrystals by simultaneous dual-surface passivation," *ACS Energy Lett.* **3**, 2301–2307 (2018).
55. D. Kim, H. Ryu, S. Y. Lim, *et al.*, "On the origin of room-temperature amplified spontaneous emission in CsPbBr<sub>3</sub> single crystals," *Chem. Mater.* **33**, 7185–7193 (2021).
56. M. B. Price, J. Butkus, T. C. Jellicoe, *et al.*, "Hot-carrier cooling and photoinduced refractive index changes in organic-inorganic lead halide perovskites," *Nat. Commun.* **6**, 8420 (2015).
57. S. Cheng, Q. Chang, Z. Wang, *et al.*, "Observation of net stimulated emission in CsPbBr<sub>3</sub> thin films prepared by pulsed laser deposition," *Adv. Opt. Mater.* **9**, 2100564 (2021).
58. Y. Wang, M. Zhi, Y.-Q. Chang, *et al.*, "Stable, ultralow threshold amplified spontaneous emission from CsPbBr<sub>3</sub> nanoparticles exhibiting trion gain," *Nano Lett.* **18**, 4976–4984 (2018).
59. A. Balena, A. Perulli, M. Fernandez, *et al.*, "Temperature dependence of the amplified spontaneous emission from CsPbBr<sub>3</sub> nanocrystal thin films," *J. Phys. Chem. C* **122**, 5813–5819 (2018).
60. H. L. Zhang, L. Yuan, Y. Chen, *et al.*, "Amplified spontaneous emission and random lasing using CsPbBr<sub>3</sub> quantum dot glass through controlling crystallization," *Chem. Commun.* **56**, 2853 (2020).
61. H. J. He, E. Ma, X. Y. Chen, *et al.*, "Single crystal perovskite microplate for high-order multiphoton excitation," *Small Methods* **3**, 1900396 (2019).
62. W. Yang, Y. Zhang, Y. J. Zhang, *et al.*, "Transparent Schottky photodiode based on AgNi NWs/SrTiO<sub>3</sub> contact with an ultrafast photoreponse to short-wavelength blue light and UV-shielding effect," *Adv. Funct. Mater.* **29**, 1905923 (2019).
63. L. X. Su, Y. Q. Zuo, and J. Xie, "Scalable manufacture of vertical p-GaN/n-SnO<sub>2</sub> heterostructure for self-powered ultraviolet photodetector, solar cell and dual-color light emitting diode," *InfoMat* **3**, 598 (2021).
64. K. W. Liu, J. G. Ma, J. Y. Zhang, *et al.*, "Ultraviolet photoconductive detector with high visible rejection and fast photoresponse based on ZnO thin film," *Solid State Electron.* **51**, 757–761 (2007).
65. H. J. Zhang, X. Liu, J. P. Dong, *et al.*, "Centimeter-sized inorganic lead halide perovskite CsPbBr<sub>3</sub> crystals grown by an improved solution method," *Cryst. Growth Des.* **17**, 6426–6431 (2017).
66. S. J. Cheng and H. Z. Zhong, "What happens when halide perovskites meet with water?" *J. Phys. Chem. Lett.* **13**, 2281–2290 (2022).
67. Y. Zou, W. J. Yu, H. Q. Guo, *et al.*, "A crystal capping layer for formation of black-phase FAPbI<sub>3</sub> perovskite in humid air," *Science* **385**, 161–167 (2024).